Formation of pyrite spherules from mixtures of biogenic FeS and organic compounds during experimental diagenesis

Arnaud Duverger, Sylvain Bernard, Jean-christophe Viennet, Jennyfer Miot, Vincent Busigny

Geochemistry, Geophysics, Geosystems®

AGU ADVANCING EARTH AND SPACE SCIENCE

RESEARCH ARTICLE
10.1029/2021GC010056

Key Points:

- Simulated diageneses were conducted on both biogenic and abiotic iron sulfide/phosphate systems to investigate pyrite biogenicity criteria
- Abiotic FeS precipitate evolved to submicrometric euhedral pyrite similar to single crystal texture commonly found in organic-poor sediments
- Biogenic FeS biofilm produced by sulfate-reducing bacteria evolved to micrometric pyrite spherules which should be further investigated as possible biosignature

Correspondence to:
A. Duverger,
arnaud.duverger@normalesup.org

Citation:
Duverger, A., Bernard, S., Viennet, J.-C., Miot, J., & Busigny, V. (2021). Formation of pyrite spherules from mixtures of biogenic FeS and organic compounds during experimental diagenesis. *Geochemistry, Geophysics, Geosystems*, *22*, e2021GC010056. https://doi.org/10.1029/2021GC010056

Received 21 JUL 2021
Accepted 5 OCT 2021

Formation of Pyrite Spherules From Mixtures of Biogenic FeS and Organic Compounds During Experimental Diagenesis

Arnaud Duverger[1,2], Sylvain Bernard[1], Jean-Christophe Viennet[1], Jennyfer Miot[1], and Vincent Busigny[2,3]

[1]Sorbonne Université, Muséum National d'Histoire Naturelle, UMR CNRS 7590, IRD. Institut de Minéralogie, de Physique des Matériaux et de Cosmochimie (IMPMC), Paris, France, [2]Université de Paris, Institut de Physique du Globe de Paris, CNRS, Paris, France, [3]Institut Universitaire de France, Paris, France

Abstract Pyrite (FeS_2) is the most common iron sulfide on the Earth's surface and has widely been used as a paleo-environmental proxy. Yet the information recorded by pyrite depends on whether it was formed through abiotic or biogenic routes. It is thus of importance to properly identify its origin. Here, we investigate the final morphology of pyrite produced upon a simulated diagenetic history from biogenic and abiotic iron sulfide/phosphate systems. Abiotic starting material obtained by chemical synthesis and biogenic starting material produced from pure culture of *Desulfovibrio desulfuricans* were submitted to increasing diagenetic conditions (75°C or 150°C from 1 to 10 days). Mineralogical products were characterized by X-ray diffraction and electron microscopy. For both biogenic and abiotic starting materials, the final state was characterized by the association of pyrite and lipscombite ($Fe^{2+}Fe_2^{3+}(OH)_2(PO_4)_2$), the most stable phases in these conditions. Intermediate phases such as greigite for iron sulfides and beraunite/wolfeite for iron phosphates were present in the abiotic residue but were not detected in the biogenic residue. Distinct pyrite morphologies were observed depending on the presence of organic matter. Indeed, while abiotic starting material led to the formation of submicrometric single crystals of pyrite with euhedral shapes similar to the subunits of well crystallized framboids, biogenic starting material produced micrometric spherulitic clusters of pyrite resembling the so-called pseudo-framboids. Although further experiments are required to ensure that it can be used as biosignatures, such specific morphologies, likely related to the presence of organic matter, may help recognizing biogenic pyrite in the geological record.

Plain Language Summary As microorganisms are rarely preserved in the geological record, looking for traces they left in the environment is crucial for investigating ancient life. Pyrite, the most stable and abundant iron sulfide in sedimentary rocks, has been widely suspected to entrap biological traces as its modern production in sediments relies on microbial activity. However, there are still no unambiguous criteria to determine if a pyrite originates from processes involving biology or not. Here we studied the evolution of iron sulfide minerals of biologic origin in comparison with non biological counterparts. Iron sulfide biofilm (rich in organic compounds) produced by bacteria versus iron sulfide particulates (without organic compounds) precipitated chemically were both heated at 75°C or 150°C for 1–10 days to simulate a geological history. Both biological and non-biological initial iron sulfides turned into pyrite during the experiments. However, the presence or absence of organic compounds induced two distinct pyrite morphologies. While pyrite particles obtained from biological iron sulfides were micrometric spherulitic clusters, non biological counterparts were submicrometric octahedral crystals. These results are important because similar morphological differences are commonly reported for natural pyrite. Spherulitic clusters may potentially suggest a biological origin for sedimentary pyrite.

1. Introduction

In natural settings, pyrite displays a wide range of morphologies that can be clustered into two main families: single crystals and framboids (Taylor & Macquaker, 2000). Pyrite single crystals are euhedral crystals (cubic, octahedral or pyritohedral shapes and their intermediates), generally ranging from hundreds of nanometers to tens of microns (Taylor & Macquaker, 2000; P. Wang et al., 2013). They occur in clusters

rather than as isolated crystals, likely because the precipitation of pyrite requires high concentrations of Fe^{2+} and S^{2-} to reach supersaturation levels, leading to multiple nucleation (Rickard, 2012). While euhedral pyrite is commonly found in organic-poor sediments, pyrite framboids are rather observed in organic-rich sediments (Bernard & Horsfield, 2014; Bernard et al., 2012; Taylor & Macquaker, 2000). A number of studies also reported pyrite framboids in fossil-rich rocks (Bernard et al., 2010; Cai et al., 2012; Grimes et al., 2002; Jauvion et al., 2020; Schallreuter, 1984) and even on carcasses having experienced decomposition in the laboratory (Vietti et al., 2015).

Framboidal pyrite is made of "microscopic spheroidal to sub-spheroidal clusters of equidimensional and equimorphic microcrystals" (Ohfuji & Rickard, 2005). It represents the dominant form of pyrite in sedimentary rocks. The formation of pyrite framboids is often assumed to involve four steps: (a) precipitation of microcrystals of FeS, (b) transformation of FeS into greigite (Fe_3S_4), (c) aggregation of greigite crystals as framboids driven by their magnetic properties, and (d) conversion of greigite into more thermodynamically stable pyrite (Wilkin & Barnes, 1997a). Alternative models for framboids formation involve the dissolution of FeS and subsequent pyrite precipitation from aqueous FeS reaction with H_2S without greigite intermediate step (Butler & Rickard, 2000). Many sedimentary pyrite spherules that do not fit the proper definition of framboids are designated by a plethora of names such as "proto-framboids" (Large et al., 2001), "packed framboids" (Sawlowicz, 1993), "welded-spheres" (Wilkin & Barnes, 1997b; Wilkin et al., 1996), "infilled framboids" (Böttcher & Lepland, 2000; Bryant et al., 2020; Wilkin & Arthur, 2001; Wilkin et al., 1996, 1997), "framboid ghosts" (Wei et al., 2012), or "united framboids" (Sugawara et al., 2013).

The origin of pyrite framboids has fueled discussions for almost a century. Historically, pyrite spherules composed of packed individual particles were assumed to be fossilized microbial communities because of similarity with sulfate-reducing bacteria colonies (Schneiderhöhn, 1923). The term framboid, derived from the French "framboise" for raspberry, was then introduced (Rust, 1935), and an abiotic origin was proposed to explain such a specific texture. Two decades later, the organic content of framboids revived the debate (Love, 1957), until it was eventually estimated to be too low to be attributed to the presence of fossilized microorganisms (Vallentyne, 1963). This idea is still present in the modern literature (Folk, 2005; Gong et al., 2008) but has been strongly challenged by the formation of framboidal pyrite in non-sedimentary environments (Scott et al., 2009) and in many laboratory syntheses under abiotic conditions (Berner, 1969; Ohfuji & Rickard, 2005; Sweeney & Kaplan, 1973; Q. Wang & Morse, 1996). Thus, biological activity should no longer be considered as a necessary prerequisite for framboidal arrangement. In detail, the link between pyrite framboids and organic matter may be more subtle. Intimate association between framboidal crystals and organic matrix has been used to suggest that biofilm could act as a template for nucleation and growth of some pyrite framboids (Large et al., 2001; Maclean et al., 2008; Wacey et al., 2015).

As biogenic pyrite is difficult to obtain in laboratory culture, the influence of microorganisms on the formation of pyrite is barely understood. Most biomineralization experiments using sulfate-reducing bacteria (SRB) reported the formation of mackinawite and greigite rather than pyrite in the presence of aqueous iron (Fortin et al., 1994; Herbert et al., 1998; Ikogou et al., 2017; Picard et al., 2018; Williams et al., 2005) or iron-minerals (Gramp et al., 2009; 2010; Ivarson & Hallberg, 1976; Neal et al., 2001). The rare pyrite produced in laboratory cultures were not framboids (Berg et al., 2020; Donald & Southam, 1999; Duverger et al., 2020; Rickard, 1969; Thiel et al., 2019). In two companion studies, both enrichment and monospecific cultures of SRB supplied with nanoparticulate iron phosphate revealed the formation of pyrite spherules only in long-lasting experiments (Berg et al., 2020; Duverger et al., 2020). Detailed monitoring of *Desulfovibrio desulfuricans* supplied with nanoparticulate iron phosphate showed an initial precipitation of a FeS biofilm. Then pyrite spherules nucleated from the biofilm after a month when all the electron donors were consumed and SRB were presumably inactive. This raises the following question: did pyrite spherules result from SRB activity or from the evolution of the biogenic FeS biofilm through diagenetic processes? Moreover, would abiotic FeS lead to the formation of the same morphology or can pyrite spherules be considered as a biosignature?

In the present study, we investigated the evolution of biogenic iron sulfide minerals in a series of experiments simulating burial diagenesis in the laboratory. Abiotic equivalents were also performed for comparison. Mixtures of iron sulfide and iron phosphate minerals resulting from SRB cultures or abiotic chemical precipitations were experimentally submitted to 75°C and 150°C for 1–10 days. The experimental products

were characterized by a combination of X-ray diffraction (XRD) and both scanning and transmission electron microscopies (SEM and TEM) coupled to energy-dispersive X-ray spectroscopy (EDS) to determine their mineral assemblage. Particular attention was paid to crystal chemistry, morphology and size. Upon simulated diagenesis, both abiotic and biogenic starting materials led to the formation of pyrite and lipscombite-like crystals ($Fe^{2+}Fe_2^{3+}(OH)_2(PO_4)_2$). However, the most important result is that pyrite occurred as euhedral single crystals in abiotic batches versus spherulitic clusters in biogenic ones, evidencing the major influence of organic compounds in the formation of pyrite spherules.

2. Materials and Methods

Milli-Q water used for syntheses and cultures was deoxygenated by bubbling N_2 (Air Liquide-Alphagaz 1) at 80°C for 45 min. All manipulations were performed in an atmosphere free of O_2 (<5 ppm) within a Jacomex® glove box filled with Ar (Air Liquide-Alphagaz 1).

2.1. Starting Materials

Biogenic material corresponds to the solid fraction of a 10-day biomineralization culture of *Desulfovibrio desulfuricans* DSM642 (DSMZ, Germany) (Beijerinck, 1895) supplied with 10 mM nanoparticulate ferric phosphate (abbreviated to FP) (Duverger et al., 2020). Briefly, the biomineralization medium was composed of 2.84 g L^{-1} Na_2SO_4, 1 mL L^{-1} trace element solution (Widdel et al., 1983), 1 mL L^{-1} selenite-tungstate solution (Tschech & Pfennig, 1984), 10 mL L^{-1} vitamin solution (Wolin et al., 1963), 20 mM sodium DL-lactate and 3 g L^{-1} MOPS ($C_7H_{15}NO_4S$) buffered to pH 7.2 with sodium hydroxide (NaOH). Bacteria were transferred at 50% (v/v), roughly equivalent to a final concentration of 5×10^7 cells mL^{-1}, to 100-mL vials sealed with butyl rubber stoppers, and stored in the dark at 30°C without stirring. After 10 days, a 15-mL volume of culture was centrifuged and rinsed three times with deoxygenated Milli-Q water to eliminate any dissolved compound. The pellet consisted essentially from the remaining FP, bacteria cells and the FeS they produced (see detailed description in the result part).

Abiotic equivalents (free of bacteria/organic matter) were prepared by mixing 20 mM iron sulfide (FeS, 87.92 g mol^{-1}) with 20 mM FP ($FePO_4 \cdot 3\,H_2O$, 204.87 g mol^{-1}). Iron sulfide was prepared by reacting 2.78 g L^{-1} $FeSO_4 \cdot 7$ H2O and 2.40 g L^{-1} $Na_2S \cdot 9\,H_2O$ (Donald & Southam, 1999). A black precipitate instantly formed and was recovered by centrifugation, rinsed three times with deoxygenated Milli-Q water and then dried in a dessicator. Nanoparticulate ferric phosphate was synthesized in ambient air by adding 5.56 g L^{-1} $FeSO_4 \cdot 7$H2O to a 2.72 g L^{-1} KH_2PO_4, 0.1 M Na-acetate solution buffered to pH 4.6 (Mirvaux et al., 2016). The greenish precipitate was recovered by centrifugation and rinsed three times with Milli-Q water. It turned yellow upon drying under oxic condition (air) at 50°C.

2.2. Experimental Diagenesis

Biogenic and abiotic starting materials were resuspended in 15 mL of deoxygenated Milli-Q water within a 23-mL PARR® PTFE Cups (A280AC). Reactors were mounted in appropriate PARR® sealed pressure vessels (4749) designed for hydrothermal synthesis. Vessels were then placed in MEMMERT® ovens (UN300) at 75°C or 150°C for 1–10 days to mimic burial diagenesis. At the end of experiments, vessels were cooled down to room temperature then transferred back to the glove box to prepare the residues for further analyses. All experiments were conducted at least twice to ensure reproducibility. Abiotic replicates were repeated with the same batch of starting material while biogenic ones were restarted from the cultivation process.

2.3. Mineralogical Characterization

2.3.1. Preparation of Residues

At the end of the experiments, 100 µL of each residue were filtered through a polycarbonate GTTP 0.2 µm filter (Merck Millipore, Darmstadt, Germany) and rinsed with 10 mL of deoxygenated Milli-Q water. Filters were mounted onto pin stubs with adhesive carbon tape before being carbon coated for SEM observations. Leftovers were collected by centrifugation at 7,000 g for 10 min and rinsed three times with deoxygenated

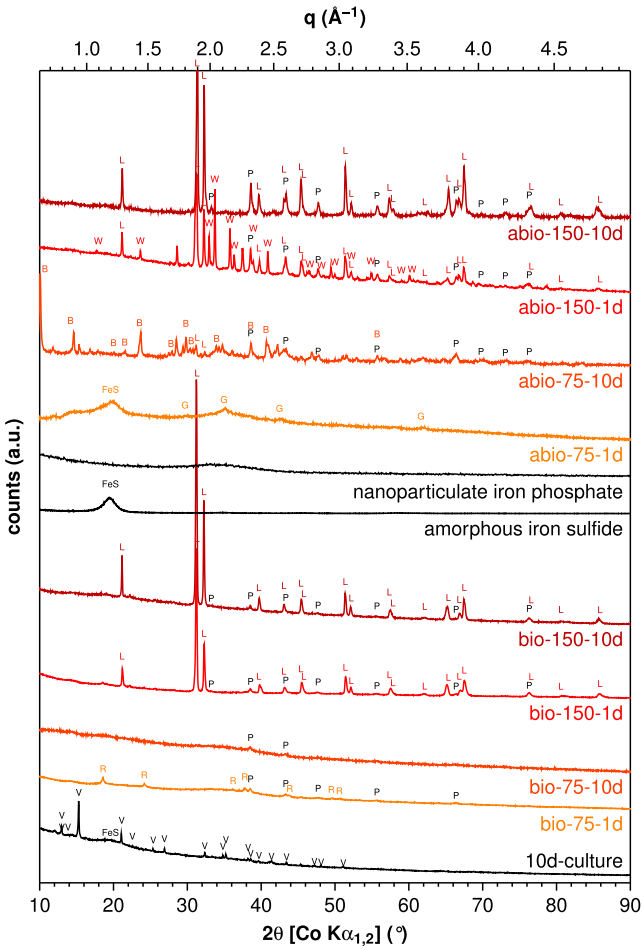

Figure 1. X-ray diffractograms of starting materials (black) and experimental diagenesis products (light orange: 75°C for 1 day, orange: 75°C for 10 days, red: 150°C for 1 day, dark red: 150°C for 10 days). Identified peaks are labeled with FeS (amorphous iron sulfide), V (vivianite, COD ID: 1001782), P (pyrite, COD ID: 5000115), R (rokühnite, COD ID: 9012466), L (pseudo-lipscombite "barb137," COD ID: 1521895), G (greigite, COD ID: 9000123), B (beraunite, COD ID: 2310377), W (wolfeite, COD ID: 9013404).

Milli-Q water. Parts of these leftovers were deposited either on a Si(111) wafer for XRD characterizations or on a 200-mesh Formvar carbon copper grid (Agar Scientific, United Kingdom) for TEM investigations. All preparations were left to dry overnight in the glove box then stored at 4°C under anoxic conditions until analysis.

2.3.2. X-Ray Diffraction

XRD characterizations were performed under an anoxic atmosphere thanks to an airtight chamber mounted on the PANalytical X'Pert Pro MPD diffractometer operating at IMPMC equipped with a cobalt anode and an X'celerator® detector positioned in Bragg-Brentano configuration. Diffractograms were acquired using a Co $K\alpha_{1,2}$ radiation (40 kV, 40 mA) from 5 to 95° 2θ angle with an increment step of 0.033°. XRD data were processed with xrayutilities Python library (Kriegner et al., 2013). Peaks were indexed by comparison with reference patterns available from the Crystallography Open Database (COD) (Gražulis et al., 2012).

2.3.3. Electron Microscopy

SEM observations were performed on the Zeiss Ultra 55 SEM operating at IMPMC equipped with a field emission gun (FEG) and a Bruker EDS Quantax detector (Bruker Corporation, Houston, TX, USA). Images were collected using an acceleration voltage of 3 kV at a working distance of 3 mm either with an Everhart Thornley detector (secondary electrons), a high performance annular detector (secondary electrons) or an annular detector with filter grid (backscattered electrons). EDS datacubes were acquired at 15 kV and 7.5 mm.

TEM investigations were achieved using the 200 kV JEOL 2100F TEM operating at IMPMC equipped with a field emission gun (FEG). Mineral identification was completed by selected-area electron diffraction (SAED). Elemental mapping was performed using EDS in the high-angle annular dark field scanning transmission electron microscopy (HAADF-STEM) mode.

3. Results

3.1. Starting Materials

The abiotic starting material was mainly X-ray amorphous, as evidenced by the slight bulging between 3.46 and 2.62 Å d-spacings (1.8 and 2.4 $Å^{-1}$ q values) on the diffractogram (Figure 1). SEM observations revealed that this material contained large aggregates of submicrometric spherules of amorphous iron phosphate (FP) (Figure 2a). Although FP was produced as $FePO_4 \cdot 3\ H_2O$, EDS spectra revealed the presence of Na and K, likely coming from the initial reactants (Figure 2d). The iron sulfide (FeS) component of this abiotic starting material consisted of amorphous FeS as indicated by the broad peak at about 5.03 Å d-spacing (1.2 $Å^{-1}$ q value) on the diffractogram (Figure 1) distributed as micrometric aggregates of indistinguishable submicrometric particles (Figures 2b and 2d). The biogenic starting material was similar to the 1 week-old culture previously described (Duverger et al., 2020) and contained micrometric aggregates of ferric phosphate (Figures 2c and 2d), some ferrous phosphate (in the form of vivianite $Fe_3(PO_4)_2 \cdot 8H_2O$) produced by the activity of SRB (Figure 1), and a biofilm-like mass of amorphous iron sulfide radically different from the abiotic FeS particles (Figures 1, 2c, and 2d). Interestingly, SRB cells could be observed in this FeS film (Figure 2c).

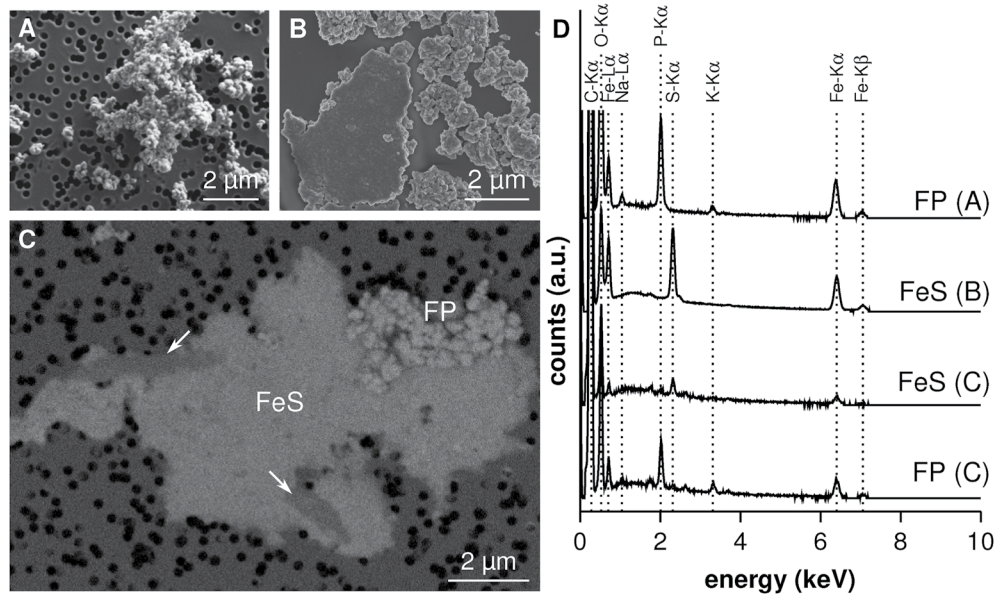

Figure 2. Scanning electron microscopy (SEM) observations of starting materials. (a, b) Secondary electron images of nanoparticulate iron phosphate (a) and iron sulfide (b) particles. (c) Backscattered electron image of biomineralization products of 10 day-old culture. White arrows point at bacteria. (d) Energy dispersive X-ray spectrometry spectra of corresponding SEM images.

3.2. Evolution of the Abiotic Starting Material

After 1 day at 75°C, the abiotic residue exhibited a diffractogram pattern typical of amorphous material (Figure 1), besides a broad peak around 5.03 Å d-spacing (1.2 $Å^{-1}$ q value) indicating that amorphous FeS was still present and a few broad peaks that could be attributed to poorly crystallized greigite (Fe_3S_4). SEM investigations revealed that the iron sulfide component did not change that much during the experiment (Figure 3a) while the initial FP exhibited nanometric dissolution holes (Figure 4a).

After 10 days at 75°C, the abiotic residue contained a number of crystallized phases as revealed by the peaks on the diffractogram, some of which indicated the presence of pyrite and remnant greigite (Figure 1). Besides masses of aggregated FP particles (Figure 4b), this residue indeed contained pyrite occurring as small (100–200 nm) euhedral (principally octahedral) crystals found either isolated (Figure 3c) or at the surface of large bi-pyramidal, sheet-like iron phosphate crystals (Figure 4c), possibly responsible for the other XRD peaks. The most intense low angle peaks on the diffractogram could correspond to beraunite ($Fe^{2+}Fe^{3+}_5(PO_4)_4(OH)_5 \cdot 6H_2O$) or whitmoreite ($Fe^{2+}Fe^{3+}_2(OH)_2(PO_4)_2 \cdot 4H_2O$, chemically equivalent to a tetrahydrated lipscombite), both mixed-valence iron hydroxyphosphates found in natural environments as alteration products (Frost et al., 2014). The two small peaks between 3.32 and 3.21 Å d-spacings (1.85 and 2 $Å^{-1}$ q values) could match a pseudo-lipscombite. The lipscombite-like reference (barb137) is a member of the solid solution series between $Fe^{2+}Fe^{3+}(PO_4)O$ and $Fe^{3+}_4(PO_4)_3(OH)_3$ with a crystal structure close to lipscombite ($Fe^{2+}Fe^{3+}_2(OH)_2(PO_4)_2$) (Schmid-Beurmann, 2000).

After 1 day at 150°C, pyrite, pseudo-lipscombite, and wolfeite ($Fe^{2+}_2(PO_4)(OH)$) were present in the abiotic residue, as evidenced by XRD (Figure 1). Pyrite displayed euhedral morphology similar to that observed after 10 days at 75°C, although individual crystals were generally larger (300–500 nm) (Figure 3e). It was distributed either isolated or associated with iron phosphate crystals (Figures 3e, 4f, and 4g). Two distinct morphologies of iron phosphate were observed, potentially explaining the XRD signal. Assuming that large bi-pyramidal crystals were pseudo-lipscombite (Figure 4g) as in the 10 days experiment (see next paragraph), the rod-shaped iron phosphate crystals could be identified as wolfeite (Figure 4f).

After 10 days at 150°C, the abiotic residue only displayed submicrometric euhedral pyrite crystals and large bi-pyramidal pseudo-lipscombite particles (Figures 3g and 4j), as also attested by XRD (Figure 1). While euhedral pyrite crystals had the same size than after 1 day at 150°C, pseudo-lipscombite particles were larger.

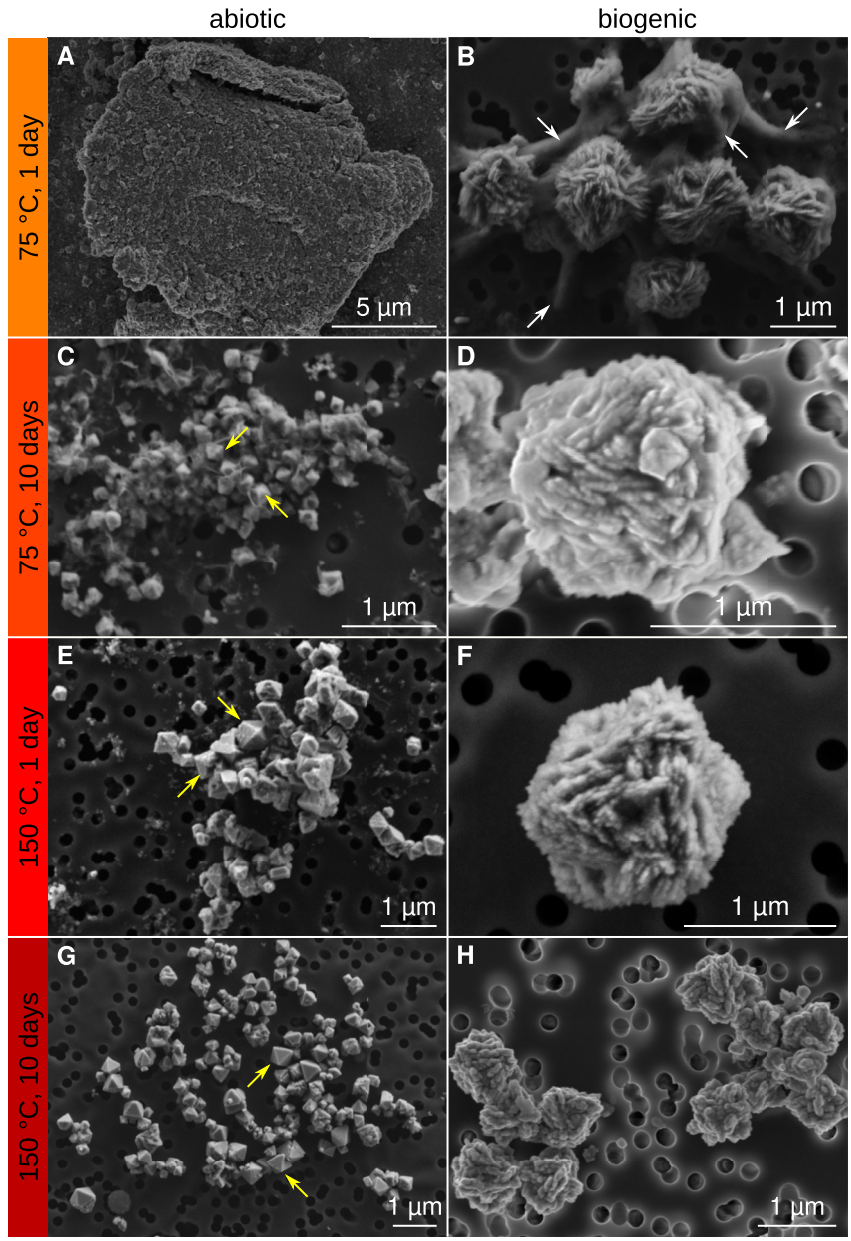

Figure 3. Secondary electron images of iron sulfides morphology. (a) Iron sulfide particle. (c, e, g) Submicrometric euhedral pyrite crystals. (b, d, f, h) Micrometric pyrite spherules. Yellow and white arrows point respectively at euhedral pyrite crystals and bacteria.

3.3. Evolution of the Biogenic Starting Material

After 1 day at 75°C, the biogenic residue mainly contained amorphous phases as shown by XRD (Figure 1). The slight bulging between 3.46 and 2.62 Å d-spacings (1.8 and 2.4 $Å^{-1}$ q values) suggested the presence of the initial FP even though no particle could be observed on SEM images (Figure 3b). However, small peaks on diffractograms suggested the presence of pyrite and rokühnite ($FeCl_2 \cdot 2H_2O$). As rokühnite is a chloride salt with a high solubility coefficient, it seems unlikely to be an experimental product and may rather be considered as a drying artifact. Interestingly, the only bacteria observed in the biogenic residue were closely associated with pyrite as revealed by SEM observations (Figure 3b). Pyrite exhibited a radically different morphology than those observed in the abiotic residues: instead of submicrometric euhedral crystals, pyrite appeared as micrometric spherulitic clusters (Figure 3b). Bacteria cells were abundant and appeared

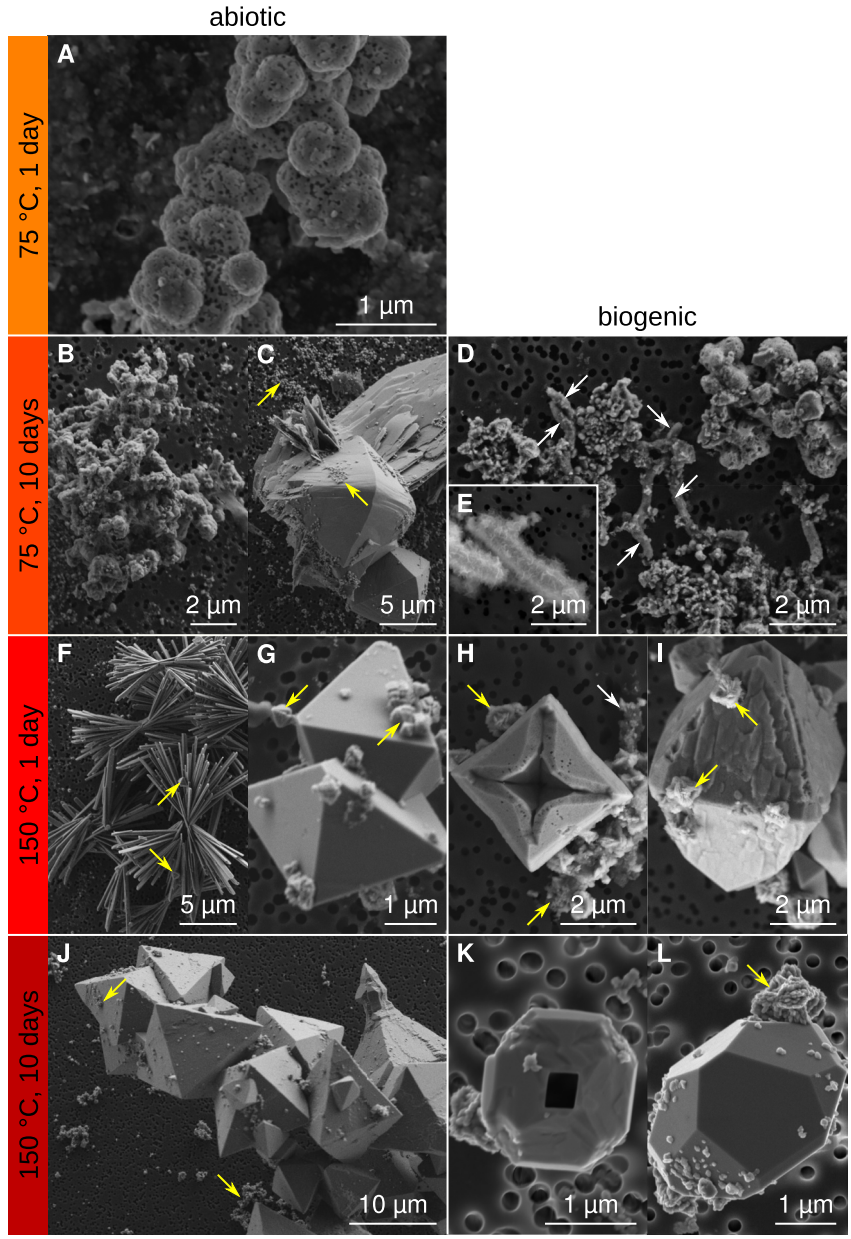

Figure 4. Secondary electron images of iron phosphate morphology. (a, b, d) Altered initial FP. (c) Association of sheet-like and bi-pyramidal iron phosphates. (e) Encrusted bacteria. (f) Rod-like iron phosphates. (g–l) Bi-pyramidal lipscombite-like minerals. Yellow arrows point at examples of pyrite crystals on iron phosphate minerals. White arrows point at bacteria.

undamaged, illustrating their good preservation under these conditions. No cell encrustation was observed at this stage.

After 10 days at 75°C, pyrite peaks were barely discernible on the diffractogram (Figure 1). As after 1 day, the biogenic residue still contained some of the initial FP, as attested by the slight bulging between 3.46 and 2.62 Å d-spacings (1.8 and 2.4 $Å^{-1}$ q values) on the diffractogram (Figure 1), and iron phosphate precipitates were observed on SEM images (Figure 4d). Micrometric pyrite spherules were still present, scattered within iron phosphate precipitates (Figure 3d). Bacteria cells were again abundant and seemed well preserved (Figure 4d). Some bacteria exhibited a spotted aspect, likely due to iron phosphate precipitated on their surface as indicated by EDS (Figures 5a, 5b, and 5e). Specifically, some cells looked encrusted in a thin iron

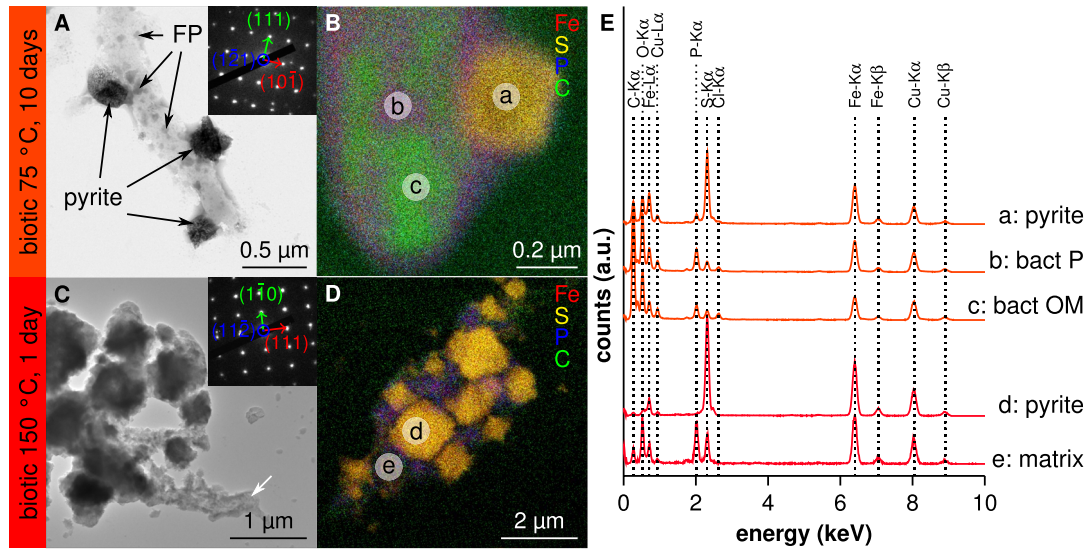

Figure 5. Transmission electron microscopy (TEM) observations of 75°C 10-day (a, b) and 150°C 1-day (c, d) experimental diagenesis products. (a) TEM image of pyrite crystals associated with a bacterium, inset displays a selected-area electron diffraction characteristic of pyrite. RGB basis is built by (101), (111) planes and ⟨121⟩ zone axis. (b) Energy dispersive X-ray spectrometry map of a pyrite associated with a bacterium. (c) TEM image of a cluster of pyrite, inset displays a selected-area electron diffraction characteristic of pyrite. RGB basis is built by (111), (110) planes and ⟨112⟩ zone axis. The white arrow points at a possible bacterium residue. (d) Energy dispersive X-ray spectrometry map of a cluster of pyrite. (e) Energy dispersive X-ray spectrometry spectra corresponding to letters in (b, d).

phosphate layer (Figure 5b) and some rod-shaped iron phosphate particles resembled cell-wall encrusted bacteria (Figure 4e). TEM investigations revealed the presence of well crystallized pyrite nuclei at the surface of bacteria cell walls (Figures 5a, 5b, and 5e).

After 1 day at 150°C, the biogenic residue was dominated by pyrite and pseudo-lipscombite (Figure 1). While pyrite spherules had a clustered aspect similar to those of the biogenic residues produced at 75°C, pseudo-lipscombite showed bi-pyramidal morphology as observed in the abiotic residues (Figures 3f, 4h, and 4i). TEM investigations evidenced that pyrite grains were either directly linked to one another or separated by an iron phosphate matrix (Figures 5d and 5e). Bacteria cells were sparsely found associated with pyrite clusters (Figures 4h and 5c).

After 10 days at 150°C, both XRD and SEM analyses provided results similar to those obtained for the biogenic residue produced after 1 day at 150°C (Figures 1, 3h, 4k, and 4l), the only significant difference being the absence of visible bacterial cells.

For all biogenic conditions, the size of pyrite spherules ranged from 0.2 to 2 µm with most of them near 1 µm. No significant size evolution was noted with increasing duration and/or temperature.

4. Discussion

4.1. Mineralogical Evolution During Simulated Burial Diagenesis

Experimental conditions (75°C/1 day, 75°C/10 days, 150°C/1 day, 150°C/10 days) were chosen to mimic natural conditions as done in previous studies. Strictly speaking, temperatures of 75°C and 150°C are reached at depths of 2.5 and 5 km in natural settings (assuming a classical geothermal gradient of 30°C km^{-1}) and thus correspond to a relatively thick burial. However, it is commonly assumed that such short-term high-temperature conditions roughly approximate long-term lower-temperature conditions, making them appropriate conditions to mimic burial diagenesis processes (Alleon et al., 2017; Alleon, Bernard, Le Guillou, Daval, et al., 2016; Bernard et al., 2015; Beveridge et al., 1983; Criouet et al., 2021; Jacquemot et al., 2019; Köhler et al., 2013; Miot et al., 2017; Picard et al., 2015; Viennet et al., 2019, 2020).

In the present experiments, both the abiotic and biogenic starting materials led to residues containing the same mineral assemblage: pyrite (at 75 and 150°C) and lipscombite (150°C), consistently with thermodynamic predictions and environmental observations. Indeed, pyrite (FeS_2) is the most stable iron sulfide (Schoonen, 2004) and is widely found in sediments (Rickard et al., 2017). Vivianite ($Fe_3(PO_4)_2 \cdot 8H_2O$) is the most stable iron phosphate in non-euxinic surface environments (Nriagu, 1972; Rothe et al., 2016). With high concentration of phosphate, vivianite precipitation can compete with iron sulfide precipitation which explains its presence in biogenic starting material (Figure 1) (Nriagu, 1972). However, lipscombite ($Fe_3(PO_4)_2(OH)_2$), beraunite ($Fe^{2+}Fe_5^{3+}(PO_4)_4(OH)_5 \cdot 6H_2O$) or rockbridgite ($Fe_5(PO_4)_3(OH)_5$) are also stable and the most likely products that can be derived from vivianite oxidation (Nriagu & Dell, 1974). As a consequence, lipscombite is widely found where iron phosphate experienced diagenetic processes like in the present experiments. As pyrite is more oxidized than the initial FeS and lipscombite is less oxidized than the initial FP, the evolution of both the abiotic and biogenic starting materials might be explained, at first order, by a single redox reaction as follow:

$$2\,FeS + 2\,FePO_4 \cdot 3\,H_2O \rightarrow FeS_2 + Fe_3\left(PO4\right)_2\left(OH\right)_2 + H_2 + 4\,H_2O. \quad (1)$$

Yet, there are significant differences between the present study results and this simplified equation. For instance, the residues produced from the abiotic starting material revealed the formation of intermediate phases for both sulfides (greigite) and phosphates (beraunite, wolfeite) before the development of pyrite and lipscombite association. In contrast, all the residues produced from the biogenic starting material contained pyrite, even the one produced after 1 day at 75°C, but none displayed greigite, beraunite nor wolfeite (Figure 1), the latter two being common alteration products (Dill et al., 2008). Although the final solution has not been collected and analyzed after the experiments, the presence of rokühnite ($FeCl_2 \cdot 2H_2O$) suggests that dissolved iron was present, consistently with the (partial to total) dissolution of the initial FP (Figures 3b and 4a) and the conversion of the initial FeS (Fe/S = 1) into pyrite (Fe/S = 0.5). This also suggests that the formation of new phosphate phases resulted from dissolution/precipitation processes rather than from a solid-state transformation. In natural environments, iron phosphates such as libscombite, wolfeite, and beraunite have frequently been reported in pegmatite (Dill, 2015; Dill et al., 2008; Robles et al., 1998; Włodek et al., 2015) and occasionally in sedimentary rocks (Dill et al., 2009; Medrano & Piper, 1997). These phases correspond to secondary phosphate minerals generated from alteration of primary phosphate with hydrothermal and/or meteoric fluids. Interestingly, beraunite and wolfeite were attributed to low and high alteration temperatures respectively (Dill et al., 2009; Włodek et al., 2015), in good agreement with the present experimental results. Indeed, beraunite was only observed at 75°C after 10 days while wolfeite occurred at 150°C after 1 day (Figure 1).

A main difference between the biogenic and abiotic starting materials resides in the nature of the FeS used. While the FeS was added as micrometric precipitates in the abiotic starting material (Figure 2b), it was present as a biofilm in the biogenic one (Figure 2c). As a consequence, abiotic and biogenic FeS exhibited different reactive surface areas, which likely influenced their rate of dissolution and/or oxidation to pyrite. In the experiment conducted with the abiotic starting material, the smaller surface area of starting FeS particles would have induced a slower oxidation rate, consistent with the detection of intermediate phases such as greigite. In the experiments conducted with the biogenic starting material, the absence of greigite may reflect a faster transformation to pyrite. Interestingly, the pyrite spherules produced during these experiments are similar to proto-framboids described as spherical structures with indistinct crystallites (Large et al., 2001). Because of their Fe/S values, these proto-framboids were suggested to represent an intermediate stage between greigite and pyrite (Large et al., 2001), consistently with the 4-step model of framboid formation (Wilkin & Barnes, 1997b). Alternatively, the absence of intermediate greigite in the residues produced from the biogenic starting material could be explained by direct precipitation of pyrite spherules from FeS (without greigite step) as observed for abiotic precipitation of (proto)framboids (Butler & Rickard, 2000). Direct transformation of FeS to pyrite is also supported by the pure pyrite single-crystal patterns of the spherules found here in the residues produced from the biogenic starting material (Figures 5a and 5c). Indeed, pyrite obtained by a transformation through a greigite step presents polycrystalline patterns with relic of greigite patterns (Berg et al., 2020).

While the initial FP was fully oxidized in the abiotic starting material, it has been at least partially reduced to vivianite (due to former SRB activity) in the biogenic starting material (Figure 1). The disappearance of

vivianite during the experiments can be explained by its oxidation and dissolution/reprecipitation as an amorphous phase (at 75°C, Figures 1, 4d, and 4e) or as lipscombite (at 150°C, Figures 1, 4h, 4i, 4k, and 4l), otherwise it would have evolved into metavivianite (Miot et al., 2009; Rothe et al., 2014).

Despite the presence of bacteria in the biogenic starting material, SRB activity is unlikely to occur as cells were transferred into a sulfate/lactate free medium for diagenetic experiments. Moreover, *Desulfovibrio desulfuricans* is not supposed to be active at temperature higher than 45°C (Bale et al., 1997). Therefore the main difference between the biogenic and abiotic starting materials resides in the presence of biogenic organic compounds (but not of active cells) in the biogenic starting material (dead bacteria cells and/or exopolymeric substances produced by SRB). The presence of these organic compounds might have accelerated the formation of lipscombite, explaining the absence of intermediate iron phosphate minerals in the biogenic residues (Figure 1). In fact, lipscombite nucleation and growth were shown to be strongly influenced by the abundance of organic compounds relative to that of FP minerals during the experimental maturation of Archaea (Miot et al., 2017). Cell walls and EPS could provide a large number of nucleation sites (Beveridge, 1989; Ferris et al., 1987) for lipscombite and pyrite, hence increasing nucleation rate, consistent with the absence of intermediate phases. Such a nucleation at the surface of cell walls and EPS is well illustrated by the precipitation of iron phosphate at cell surface (Figure 4e) and by the pyrite crystals blooming on SRB cells (Figures 3b and 5a–5c).

Moreover, organic matter oxidation is known to be promoted by Fe-bearing phases (McCollom, 2013). Therefore, the reduction of initial FP into lipscombite may have been driven only by the oxidation of FeS into pyrite during the experiments conducted with the abiotic starting material. In contrast, it was likely promoted by a combination of FeS oxidation to pyrite and organic compounds oxidation during the experiments conducted with the biogenic starting material. Further analyses of organic matter content, fluid and gas compositions might be useful to test this hypothesis.

4.2. Comparison With Natural Environments

The pyrite produced here exhibited significant differences in size and morphology. While all the pyrite particles produced during experiments conducted with the abiotic starting material were well-crystallized submicrometric octahedral grains (Figures 1, 3c, 3e, and 3g), the pyrite particles produced during experiments conducted with the biogenic starting material were poorly crystallized, micrometer-scale, spherulitic clusters (Figures 1, 3b, 3d, 3f, and 3h). Of note, although these pyrite spherules share similarities with framboids, they cannot be considered as true framboids because of the lack of distinct crystallites, as in the case of a number of sedimentary pyrites that look like plain spherules sometimes exhibiting surface ornaments (Sawlowicz, 1993; Wei et al., 2012; Wilkin & Barnes, 1997b). However, the single-crystalline selected-area electron diffraction patterns of the smallest spherules produced from biogenic starting material revealed they had an internal structure (Figures 5a and 5c), while biogenic pyrite spherules produced from cultures have been described as polycrystalline (Berg et al., 2020; Duverger et al., 2020). Crystallographic ordering might result from a burial induced close-packing effect (Sawłowicz, 2000).

Sedimentary pyrites display essentially two types of morphologies: euhedral single crystals and framboids, the latter including a number of spherical framboid-like objects with indistinct crystallites. Both types of pyrite morphologies were reported in the Lower Jurassic Cleveland Ironstone Formation of eastern England (Taylor & Macquaker, 2000): while pyrite framboids were observed in organic-rich clay/silt mudstones, euhedral pyrite crystals were found in sand-rich mudstones with a lower organic content. A similar result was obtained in the present study since euhedral pyrite crystals were produced during experiments conducted with the abiotic starting material (in the absence of organic compounds) while pyrite spherules were produced during experiments conducted with the biogenic starting material (in the presence of biogenic organic compounds). Interestingly, some micrometric iron sulfide spherules (probably pyrite) were commonly observed in natural sediments, but not described in previous studies focused on framboids associated with biofilm (e.g., Large et al., 2001; Maclean et al., 2008, see Figures 2f and 3a).

It is generally considered that framboids form when solutions are supersaturated with respect to both pyrite and mackinawite (Morse et al., 1987; Sweeney & Kaplan, 1973), while the precipitation of euhedral pyrite crystals does not need mackinawite supersaturation to be reached (Rickard, 1997; Q. Wang & Morse, 1996).

In natural settings, SRB activity (favored by the organic matter content) controls the rate of sulfide production, leading to supersaturation with respect to pyrite and eventually mackinawite. Yet, no SRB activity is expected under the conditions of the experiments conducted here (no sulfate/lactate and temperature >45°C). Redox conditions may also affect pyrite morphologies by influencing the supersaturation effect (Butler & Rickard, 2000). Indeed, pyrite framboids could be synthesized abiotically at high Eh (−250 mV), while only euhedral crystals were produced at lower Eh (−400 mV) (Butler & Rickard, 2000).

Here, the presence of organic compounds in the biogenic starting material might have increased the Eh value of the system, inducing the nucleation of pyrite spherules. Additionally, organic compounds could have acted as templates for spherule formation in the same way biofilms could be involved in natural framboid formation, as suggested from the study of modern mineralized biofilms from South Africa gold mine (Maclean et al., 2008) and from the study of fossilized biofilms found in Ediacarian sediments from Newfoundland (Wacey et al., 2015). It has been shown that organic compounds provide confined spaces (Maclean et al., 2008) and binding sites for cations either on cell walls (Ferris et al., 1987) or exopolymeric substances (Flemming, 1995). Altogether, these features could have triggered supersaturation with respect to both pyrite and mackinawite in the experiments conducted with the biogenic starting material and subsequent formation of pyrite spherules rather than euhedral pyrite crystals.

In natural systems, euhedral pyrite crystals may have different habits such as cube, octahedron or pyritohedron and all their intermediates (Rickard, 2012). In general, different habits coexist (Tang & Li, 2020). Lab experiments have revealed that crystal habits depend on the degree of supersaturation of the solution with respect to pyrite (Murowchick & Barnes, 1987): high supersaturation favoring the production of octahedral shapes over cubic shapes. The coexistence of different habits of pyrite in natural settings might be explained by the variable rate of sulfate-reduction which depends on the availability of organic matter and controls the supersaturation of the solution with respect to pyrite. Here, only pyrite octahedra were produced during the experiments using the abiotic starting material (Figures 3c, 3e, and 3g), likely because the solution was always supersaturated with respect to pyrite at the temperature of the experiments.

Euhedral and framboidal pyrites in natural settings also differ in size. Sedimentary euhedral pyrite grains are generally smaller than 1 μm (Taylor & Macquaker, 2000) consistently with the submicrometric pyrite crystals observed in the residues obtained from abiotic starting material (Figures 3c, 3e, and 3g). Statistical analysis of sedimentary framboids shows a larger size, with a range from 1 to more than 50 μm and a mean diameter around 5 μm (Wilkin et al., 1996). In detail, pyrite framboids average 5.0 ± 1.7 μm in euxinic (anoxic and sulfidic) sediments while those from dysoxic or oxic sediments are generally larger, with a mean diameter of 7.7 ± 4.1 μm (Wilkin et al., 1996). Oxic conditions were thus suggested to favor the production of larger pyrite framboids (Wilkin et al., 1996). By analogy, the limited size of the pyrite spherules (from 0.2 to 2 μm) produced during the experiments conducted with the biogenic starting material might be explained by the strict anoxic conditions. Still, these pyrite spherules were larger than the 100-nanometer pyrite spherules formed in a long-term culture (1 month) of *Desulfovibrio desulfuricans* supplied with FP at 30°C (Duverger et al., 2020). This difference might be explained by the temperature conditions used here (75°C and 150°C) which likely boosted the conversion of the FeS biofilm to pyrite spherules.

4.3. Pyrite Spherules: A Biosignature?

For decades, pyrite has been targeted as a potential biosignature in the geological record (Goodwin et al., 1976; Schieber, 2002; Shen et al., 2001; Zhelezinskaia et al., 2014). Biogenic pyrite grains produced via bacterial sulfate-reduction exhibit ^{34}S depleted down to 60‰ (Harrison & Thode, 1958; Sim et al., 2011), that is, values much higher than those of abiotic pyrite grains (e.g., <20‰ in thermochemical sulfate-reduction [Watanabe et al., 2009]). Therefore, the S isotope compositions of Archean pyrites have tentatively been used to infer the antiquity of bacterial sulfate-reduction, possibly ≈3.4 Ga ago (Marin-Carbonne et al., 2018; Shen et al., 2001; Wacey et al., 2011).

The same is true for morphologies. Framboidal morphologies have often been interpreted as biogenic (Love, 1957; Wacey et al., 2015) but abiotic pyrite may exhibit similar habits (Ohfuji & Rickard, 2005). Rather than true framboids, we evidenced here the production of pyrite spherules from the biogenic starting material. Similar spherulitic pyrites were reported in the literature (Bryant et al., 2020; Large et al., 2001;

Sawlowicz, 1993; Sugawara et al., 2013; Wei et al., 2012; Wilkin et al., 1996) but described using various names related to framboids, even though they differ from true framboids by their massive cores with undefined crystallites. The use of the term framboid to describe pyrites with significantly different textures, either formed in abiotic experiments (Butler & Rickard, 2000; Wolthers et al., 2005) or in the presence of bacterial biofilms (Large et al., 2001; Maclean et al., 2008; Vietti et al., 2015), complicates the discussion regarding their origin.

Here the production of spherules occurred only in the presence of organic compounds. It may thus be expected that these spherules entrapped some of these organic compounds during their formation. Provided that these compounds withstand diagenesis, a fine-scale observation of the association with organic compounds might thus help discussing the origin of framboid-like pyrite. In our simulated diagenesis, the presence of organic compounds catalyzed the formation of pyrite and lipscombite in the biogenic experiments while intermediate phases (greigite, beraunite/whitmoreite, wolfeite) were only observed in the abiotic ones (Figure 1). Future experiments should determine whether entrapment within pyrite spherules limits or promotes the chemical degradation of biogenic organic compounds upon advanced diagenesis. This will provide additional and necessary constraints to properly discuss the origin (biogenic or abiotic) of framboid-like pyrite found in natural settings. Moreover, the nature of the organic compounds potentially encrusted within these spherules will need to be investigated.

The organic compounds of the biogenic starting material consist of a mixture of lipids, sugars, proteins and nucleic acids. Besides lipids, all these compounds are poorly resistant to thermal diagenesis (Alleon et al., 2017; Bernard et al., 2015; Criouet et al., 2021; Viennet et al., 2019). Yet, amide-rich organic compounds, possibly derived from proteins, have been detected in ancient cherts as old as 3.5 Ga old (Alleon, Bernard, Le Guillou, Marin-Carbonne, et al., 2016; Alleon et al., 2018, 2021), likely thanks to their early entombment within silica (Alleon, Bernard, Le Guillou, Daval, et al., 2016). The diagenetic chemical degradation of biogenic organic compounds is also limited when encrusted in calcium phosphates (Li et al., 2014) or iron oxides (Picard et al., 2015, 2016), but this is the opposite with iron phosphates (Miot et al., 2017) or clay minerals (Jacquemot et al., 2019; Viennet et al., 2019, 2020). Future experiments should thus focus on the preservation/degradation of organic compounds associated with pyrite spherules, to eventually provide new arguments to discuss their origin.

5. Conclusion

Despite years of discussion and debates, there is still no robust criteria to establish the biogenic or abiotic origin of pyrite. In simulated diagenetic experiments, we evidenced the formation of pyrite spherules from FeS biofilms produced by SRB. While abiotic and biogenic iron sulfide/phosphate systems treatments led to the same mineralogical association of pyrite and lipscombite, abiotic set-up evolved through intermediate phases (greigite, beraunite/whitmoreite, wolfeite). Moreover, pyrite obtained from abiotic FeS devoid of organic compounds exhibited very different morphologies, that is, euhedral single crystals. Altogether, the present results suggest that pyrite spherules may potentially constitute a biosignature. Among the important remaining questions, future studies should determine whether pyrite spherules formation was controlled by the nature of the FeS biofilm inherited from former bacterial activity or the sole presence of organic compounds. This could be achieved for instance by simulated diagenesis experiments mixing various types of organic matter (including dead biomass, abiotic hydrocarbons, ...) with abiotic starting material similar to the present work. Finally, it would be interesting to explore if the two distinct pyrite morphologies (euhedral single crystal or spherulitic clusters) are characterized by specific S isotope signatures.

Data Availability Statement

All original data supporting the conclusions of this article are available in this manuscript. Crystallographic Information Files used to generate XRD reference patterns were retrieved from https://www.crystallography.net/cod/. They were processed by xrayutilities Python library (Kriegner et al., 2013) available for download at https://github.com/dkriegner/xrayutilities. Energy-dispersive X-ray spectra were processed from EDS datacube by Hyperpsy Python library (Peña et al., 2020) available for download at https://github.com/hyperspy/hyperspy.

Acknowledgments
This work was funded by the ANR SRB project, under grant ANR-14-CE33-0003-01, of the French Agence Nationale de la Recherche to JM. The authors would like to thank the staff of the IMPMC (Sorbonne Universités) for their support and training on instruments: Benoît Baptiste and Ludovic Delbès for the X-ray diffraction facility, Jean-Michel Guigner for the transmission electron microscopy facility, Imène Estéve, Béatrice Doisneau, and Stéphanie Delbrel for the scanning electron microscopy facility, and Fériel Skouri-Panet and Mélanie Poinsot for the Biology Lab. The scanning electron microscopy facility at the IMPMC is funded by Région Ile de France, under grant SESAME 2006 N°I-07-593/R, INSU/CNRS, UPMC-Paris 6, and by the Agence Nationale de la Recherche (grant N°ANR-07-BLAN-0124-01). V. Busigny thanks the Institut Universitaire de France for funding (IUF#2017–2021). The transmission electron microscopy facility at IMPMC is supported by Région Ile de France, under grant SESAME 2000 E 1435. The authors also thank two anonymous reviewers whose constructive comments substantially improved this manuscript and Joshua Feinberg for handling the manuscript.

References

Alleon, J., Bernard, S., Le Guillou, C., Beyssac, O., Sugitani, K., & Robert, F. (2018). Chemical nature of the 3.4 Ga Strelley Pool microfossils. *Geochemical Perspectives Letters*, 37–42. https://doi.org/10.7185/geochemlet.1817

Alleon, J., Bernard, S., Le Guillou, C., Daval, D., Skouri-Panet, F., Kuga, M., & Robert, F. (2017). Organic molecular heterogeneities can withstand diagenesis. *Scientific Reports*, *7*(1), 1508. https://doi.org/10.1038/s41598-017-01612-8

Alleon, J., Bernard, S., Le Guillou, C., Daval, D., Skouri-Panet, F., Pont, S., et al. (2016). Early entombment within silica minimizes the molecular degradation of microorganisms during advanced diagenesis. *Chemical Geology*, *437*, 98–108. https://doi.org/10.1016/j.chemgeo.2016.05.034

Alleon, J., Bernard, S., Le Guillou, C., Marin-Carbonne, J., Pont, S., Beyssac, O., et al. (2016). Molecular preservation of 1.88 Ga Gunflint organic microfossils as a function of temperature and mineralogy. *Nature Communications*, *7*(1), 11977. https://doi.org/10.1038/ncomms11977

Alleon, J., Bernard, S., Olivier, N., Thomazo, C., & Marin-Carbonne, J. (2021). Inherited geochemical diversity of 3.4 Ga organic films from the Buck Reef Chert, South Africa. *Communications Earth & Environment*, *2*(1), 6. https://doi.org/10.1038/s43247-020-00066-7

Bale, S. J., Goodman, K., Rochelle, P. A., Marchesi, J. R., Fry, J. C., Weightman, A. J., & Parkes, R. J. (1997). Desulfovibrio profundus sp. nov., a novel barophilic sulfate-reducing bacterium from deep sediment layers in the Japan Sea. *International Journal of Systematic Bacteriology*, *47*(2), 515–521. https://doi.org/10.1099/00207713-47-2-515

Beijerinck, M. (1895). Über Spirillum desulfuricans als ursache von sulfatreduktion. *Centralblatt für Bakteriologie und Parasitenkunde*, *1*, 1–9.

Berg, J. S., Duverger, A., Cordier, L., Laberty-Robert, C., Guyot, F., & Miot, J. (2020). Rapid pyritization in the presence of a sulfur/sulfate-reducing bacterial consortium. *Scientific Reports*, *10*(1), 8264. https://doi.org/10.1038/s41598-020-64990-6

Bernard, S., Benzerara, K., Beyssac, O., Balan, E., & Brown Jr., G. (2015). Evolution of the macromolecular structure of sporopollenin during thermal degradation. *Heliyon*, *1*(2), e00034. https://doi.org/10.1016/j.heliyon.2015.e00034

Bernard, S., Benzerara, K., Beyssac, O., & Brown, G. E. (2010). Multiscale characterization of pyritized plant tissues in blueschist facies metamorphic rocks. *Geochimica et Cosmochimica Acta*, *74*(17), 5054–5068. https://doi.org/10.1016/j.gca.2010.06.011

Bernard, S., & Horsfield, B. (2014). Thermal maturation of gas shale systems. *Annual Review of Earth and Planetary Sciences*, *42*(1), 635–651. https://doi.org/10.1146/annurev-earth-060313-054850

Bernard, S., Horsfield, B., Schulz, H.-M., Wirth, R., Schreiber, A., & Sherwood, N. (2012). Geochemical evolution of organic-rich shales with increasing maturity: A STXM and TEM study of the Posidonia Shale (Lower Toarcian, northern Germany). *Marine and Petroleum Geology*, *31*(1), 70–89. https://doi.org/10.1016/j.marpetgeo.2011.05.010

Berner, R. A. (1969). The synthesis of framboidal pyrite. *Economic Geology*, *64*(4), 383–384. https://doi.org/10.2113/gsecongeo.64.4.383

Beveridge, T. J. (1989). Role of cellular design in bacterial metal accumulation and mineralization. *Annual Review of Microbiology*, *43*(1), 147–171. https://doi.org/10.1146/annurev.mi.43.100189.001051

Beveridge, T. J., Meloche, J. D., Fyfe, W. S., & Murray, R. G. E. (1983). Diagenesis of metals chemically complexed to bacteria: Laboratory formation of metal phosphates, sulfides, and organic condensates in artificial sediments. *Applied and Environmental Microbiology*, *45*(3), 1094–1108. https://doi.org/10.1128/AEM.45.3.1094-1108.1983

Böttcher, M. E., & Lepland, A. (2000). Biogeochemistry of sulfur in a sediment core from the west-central Baltic Sea: Evidence from stable isotopes and pyrite textures. *Journal of Marine Systems*, *25*(3–4), 299–312. https://doi.org/10.1016/S0924-7963(00)00023-3

Bryant, R., Jones, C., Raven, M., Owens, J., & Fike, D. (2020). Shifting modes of iron sulfidization at the onset of OAE-2 drive regional shifts in pyrite $delta$34S records. *Chemical Geology*, *553*, 119808. https://doi.org/10.1016/j.chemgeo.2020.119808

Butler, I. B., & Rickard, D. (2000). Framboidal pyrite formation via the oxidation of iron (II) monosulfide by hydrogen sulphide. *Geochimica et Cosmochimica Acta*, *64*(15), 2665–2672. https://doi.org/10.1016/S0016-7037(00)00387-2

Cai, Y., Schiffbauer, J. D., Hua, H., & Xiao, S. (2012). Preservational modes in the Ediacaran Gaojiashan Lagerstätte: Pyritization, aluminosilicification, and carbonaceous compression. *Palaeogeography, Palaeoclimatology, Palaeoecology*, *326–328*, 109–117. https://doi.org/10.1016/j.palaeo.2012.02.009

Criouet, I., Viennet, J.-C., Jacquemot, P., Jaber, M., & Bernard, S. (2021). Abiotic formation of organic biomorphs under diagenetic conditions. *Geochemical Perspectives Letters*, *16*, 40–46. https://doi.org/10.7185/geochemlet.2102

Dill, H. G. (2015). Pegmatites and aplites: Their genetic and applied ore geology. *Ore Geology Reviews*, *69*, 417–561. https://doi.org/10.1016/j.oregeorev.2015.02.022

Dill, H. G., Melcher, F., Gerdes, A., & Weber, B. (2008). The origin and zoning of hypogene and supergene Fe-Mn-Mg-Sc-U-REE phosphate mineralization from the newly discovered trutzhofmuhle aplite, hagendorf pegmatite province, Germany. *The Canadian Mineralogist*, *46*(5), 1131–1157. https://doi.org/10.3749/canmin.46.5.1131

Dill, H. G., Weber, B., & Kaufhold, S. (2009). The origin of sideritegoethitephosphate mineralization in the karst-related faultbound iron ore deposit Auerbach, Germany, a clue to the timing of hypogene and supergene Fe-Al phosphates in NE Bavaria. *Neues Jahrbuch für Mineralogie - Abhandlungen*, *186*(3), 283–307. https://doi.org/10.1127/0077-7757/2009/0149

Donald, R., & Southam, G. (1999). Low temperature anaerobic bacterial diagenesis of ferrous monosulfide to pyrite. *Geochimica et Cosmochimica Acta*, *63*(13–14), 2019–2023. https://doi.org/10.1016/S0016-7037(99)00140-4

Duverger, A., Berg, J. S., Busigny, V., Guyot, F., Bernard, S., & Miot, J. (2020). Mechanisms of pyrite formation promoted by sulfate-reducing bacteria in pure culture. *Frontiers of Earth Science*, *8*, 588310. https://doi.org/10.3389/feart.2020.588310

Ferris, F., Fyfe, W., & Beveridge, T. (1987). Bacteria as nucleation sites for authigenic minerals in a metal-contaminated lake sediment. *Chemical Geology*, *63*(3–4), 225–232. https://doi.org/10.1016/0009-2541(87)90165-3

Flemming, H.-C. (1995). Sorption sites in biofilms. *Water Science and Technology*, *32*(8), 27–33. https://doi.org/10.2166/wst.1995.0256

Folk, R. L. (2005). Nannobacteria and the formation of framboidal pyrite: Textural evidence. *Journal of Earth System Science*, *114*(3), 369–374. https://doi.org/10.1007/BF02702955

Fortin, D., Southam, G., & Beveridge, T. (1994). Nickel sulfide, iron-nickel sulfide and iron sulfide precipitation by a newly isolated Desulfotomaculum species and its relation to nickel resistance. *FEMS Microbiology Ecology*, *14*(2), 121–132. https://doi.org/10.1111/j.1574-6941.1994.tb00099.x

Frost, R. L., López, A., Scholz, R., Xi, Y., & Lana, C. (2014). The molecular structure of the phosphate mineral beraunite $Fe^{2+}Fe^{53+}(PO_4)4(OH)5.4H_2O$—A vibrational spectroscopic study. *Spectrochimica Acta Part A: Molecular and Biomolecular Spectroscopy*, *128*, 408–412. https://doi.org/10.1016/j.saa.2014.02.198

Gong, Y.-M., Shi, G. R., Weldon, E. A., Du, Y.-S., & Xu, R. (2008). Pyrite framboids interpreted as microbial colonies within the Permian *Zoophycos* spreiten from southeastern Australia. *Geological Magazine*, *145*(1), 95–103. https://doi.org/10.1017/S0016756807003974

Goodwin, A. M., Monster, J., & Thode, H. G. (1976). Carbon and sulfur isotope abundances in Archean iron-formations and early Precambrian life. *Economic Geology*, *71*(5), 870–891. https://doi.org/10.2113/gsecongeo.71.5.870

Gramp, J. P., Bigham, J. M., Jones, F. S., & Tuovinen, O. H. (2010). Formation of Fe-sulfides in cultures of sulfate-reducing bacteria. *Journal of Hazardous Materials*, *175*(1–3), 1062–1067. https://doi.org/10.1016/j.jhazmat.2009.10.119

Gramp, J. P., Wang, H., Bigham, J. M., Jones, F. S., & Tuovinen, O. H. (2009). Biogenic Synthesis and Reduction of Fe(III)-hydroxysulfates. *Geomicrobiology Journal*, *26*(4), 275–280. https://doi.org/10.1080/01490450902892597

Gražulis, S., Daškevič, A., Merkys, A., Chateigner, D., Lutterotti, L., Quirós, M., et al. (2012). Crystallography Open Database (COD): An open-access collection of crystal structures and platform for world-wide collaboration. *Nucleic Acids Research*, *40*(D1), D420–D427. https://doi.org/10.1093/nar/gkr900

Grimes, S. T., Davies, K. L., Butler, I. B., Brock, F., Edwards, D., Rickard, D., et al. (2002). Fossil plants from the Eocene London Clay: The use of pyrite textures to determine the mechanism of pyritization. *Journal of the Geological Society*, *159*(5), 493–501. https://doi.org/10.1144/0016-764901-176

Harrison, A. G., & Thode, H. G. (1958). Mechanism of the bacterial reduction of sulphate from isotope fractionation studies. *Transactions of the Faraday Society*, *54*, 84. https://doi.org/10.1039/tf9585400084

Herbert, R. B., Benner, S. G., Pratt, A. R., & Blowes, D. W. (1998). Surface chemistry and morphology of poorly crystalline iron sulfides precipitated in media containing sulfate-reducing bacteria. *Chemical Geology*, *144*(1–2), 87–97. https://doi.org/10.1016/S0009-2541(97)00122-8

Ikogou, M., Ona-Nguema, G., Juillot, F., Le Pape, P., Menguy, N., Richeux, N., et al. (2017). Long-term sequestration of nickel in mackinawite formed by Desulfovibrio capillatus upon Fe(III)-citrate reduction in the presence of thiosulfate. *Applied Geochemistry*, *80*, 143–154. https://doi.org/10.1016/j.apgeochem.2017.02.019

Ivarson, K., & Hallberg, R. (1976). Formation of mackinawite by the microbial reduction of jarosite and its application to tidal sediments. *Geoderma*, *16*(1), 1–7. https://doi.org/10.1016/0016-7061(76)90089-6

Jacquemot, P., Viennet, J.-C., Bernard, S., Le Guillou, C., Rigaud, B., Delbes, L., et al. (2019). The degradation of organic compounds impacts the crystallization of clay minerals and vice versa. *Scientific Reports*, *9*(1), 20251. https://doi.org/10.1038/s41598-019-56756-6

Jauvion, C., Bernard, S., Gueriau, P., Mocuta, C., Pont, S., Benzerara, K., & Charbonnier, S. (2020). Exceptional preservation requires fast biodegradation: Thylacocephalan specimens from La Voulte-sur-Rhône (Callovian, Jurassic, France). *Palaeontology*, *63*(3), 395–413. https://doi.org/10.1111/pala.12456

Köhler, I., Konhauser, K. O., Papineau, D., Bekker, A., & Kappler, A. (2013). Biological carbon precursor to diagenetic siderite with spherical structures in iron formations. *Nature Communications*, *4*(1), 1741. https://doi.org/10.1038/ncomms2770

Kriegner, D., Wintersberger, E., & Stangl, J. (2013). *Xrayutilities* : A versatile tool for reciprocal space conversion of scattering data recorded with linear and area detectors. *Journal of Applied Crystallography*, *46*(4), 1162–1170. https://doi.org/10.1107/S0021889813017214

Large, D., Fortey, N., Milodowski, A., Christy, A., & Dodd, J. (2001). Petrographic observations of iron, copper, and zinc sulfides in freshwater canal sediment. *Journal of Sedimentary Research*, *71*(1), 61–69. https://doi.org/10.1306/052600710061

Li, J., Bernard, S., Benzerara, K., Beyssac, O., Allard, T., Cosmidis, J., & Moussou, J. (2014). Impact of biomineralization on the preservation of microorganisms during fossilization: An experimental perspective. *Earth and Planetary Science Letters*, *400*, 113–122. https://doi.org/10.1016/j.epsl.2014.05.031

Love, L. G. (1957). Micro-organisms and the presence of syngenetic pyrite. *Quarterly Journal of the Geological Society*, *113*(1–4), 429–440. https://doi.org/10.1144/GSL.JGS.1957.113.01-04.18

Maclean, L. C. W., Tyliszczak, T., Gilbert, P. U. P. A., Zhou, D., Pray, T. J., Onstott, T. C., & Southam, G. (2008). A high-resolution chemical and structural study of framboidal pyrite formed within a low-temperature bacterial biofilm. *Geobiology*, *6*(5), 471–480. https://doi.org/10.1111/j.1472-4669.2008.00174.x

Marin-Carbonne, J., Remusat, L., Sforna, M. C., Thomazo, C., Cartigny, P., & Philippot, P. (2018). Sulfur isotope's signal of nanopyrites enclosed in 2.7 Ga stromatolitic organic remains reveal microbial sulfate reduction. *Geobiology*, *16*(2), 121–138. https://doi.org/10.1111/gbi.12275

McCollom, T. M. (2013). The influence of minerals on decomposition of the n-alkyl-*alpha*-amino acid norvaline under hydrothermal conditions. *Geochimica et Cosmochimica Acta*, *104*, 330–357. https://doi.org/10.1016/j.gca.2012.11.008

Medrano, M. D., & Piper, D. Z. (1997). Fe–Ca-phosphate, Fe-silicate, and Mn-oxide minerals in concretions from the Monterey Formation. *Chemical Geology*, *138*(1–2), 9–23. https://doi.org/10.1016/S0009-2541(96)00170-2

Miot, J., Benzerara, K., Morin, G., Bernard, S., Beyssac, O., Larquet, E., et al. (2009). Transformation of vivianite by anaerobic nitrate-reducing iron-oxidizing bacteria. *Geobiology*, *7*(3), 373–384. https://doi.org/10.1111/j.1472-4669.2009.00203.x

Miot, J., Bernard, S., Bourreau, M., Guyot, F., & Kish, A. (2017). Experimental maturation of Archaea encrusted by Fe-phosphates. *Scientific Reports*, *7*(1), 16984. https://doi.org/10.1038/s41598-017-17111-9

Mirvaux, B., Recham, N., Miot, J., Courty, M., Bernard, S., Beyssac, O., et al. (2016). Iron phosphate/bacteria composites as precursors for textured electrode materials with enhanced electrochemical properties. *Journal of the Electrochemical Society*, *163*(10), A2139–A2148. https://doi.org/10.1149/2.0101610jes

Morse, J., Millero, F., Cornwell, J., & Rickard, D. (1987). The chemistry of the hydrogen sulfide and iron sulfide systems in natural waters. *Earth-Science Reviews*, *24*(1), 1–42. https://doi.org/10.1016/0012-8252(87)90046-8

Murowchick, J. B., & Barnes, H. L. (1987). Effects of temperature and degree of supersaturation on pyrite morphology. *American Mineralogist*, *72*(11–12), 1241–1250.

Neal, A. L., Techkarnjanaruk, S., Dohnalkova, A., McCready, D., Peyton, B. M., & Geesey, G. G. (2001). Iron sulfides and sulfur species produced at hematite surfaces in the presence of sulfate-reducing bacteria. *Geochimica et Cosmochimica Acta*, *65*(2), 223–235. https://doi.org/10.1016/S0016-7037(00)00537-8

Nriagu, J. O. (1972). Stability of vivianite and ion-pair formation in the system fe3(PO4)2-H3PO4H3PO4-H2o. *Geochimica et Cosmochimica Acta*, *36*(4), 459–470. https://doi.org/10.1016/0016-7037(72)90035-X

Nriagu, J. O., & Dell, C. I. (1974). Diagenetic formation of iron phosphates in recent lake sediments. *American Mineralogist*, *59*(9–10), 934–946.

Ohfuji, H., & Rickard, D. (2005). Experimental syntheses of framboids—A review. *Earth-Science Reviews*, *71*(3–4), 147–170. https://doi.org/10.1016/j.earscirev.2005.02.001

Peña, F. D. L., Prestat, E., Fauske, V. T., Burdet, P., Furnival, T., Jokubauskas, P., et al. (2020). *Hyperspy/hyperspy: Release v1.6.1*. Zenodo. https://doi.org/10.5281/ZENODO.4294676

Picard, A., Gartman, A., Clarke, D. R., & Girguis, P. R. (2018). Sulfate-reducing bacteria influence the nucleation and growth of mackinawite and greigite. *Geochimica et Cosmochimica Acta*, *220*, 367–384. https://doi.org/10.1016/j.gca.2017.10.006

Picard, A., Kappler, A., Schmid, G., Quaroni, L., & Obst, M. (2015). Experimental diagenesis of organo-mineral structures formed by microaerophilic Fe(II)-oxidizing bacteria. *Nature Communications*, *6*(1), 6277. https://doi.org/10.1038/ncomms7277
Picard, A., Obst, M., Schmid, G., Zeitvogel, F., & Kappler, A. (2016). Limited influence of Si on the preservation of Fe mineral-encrusted microbial cells during experimental diagenesis. *Geobiology*, *14*(3), 276–292. https://doi.org/10.1111/gbi.12171
Rickard, D. (1969). The microbiological formation of iron sulphides. *Stockholm Contributions in Geology*, *20*, 49–66.
Rickard, D. (1997). Kinetics of pyrite formation by the H2S oxidation of iron (II) monosulfide in aqueous solutions between 25 and 125°C: The rate equation. *Geochimica et Cosmochimica Acta*, *61*(1), 115–134. https://doi.org/10.1016/S0016-7037(96)00321-3
Rickard, D. (2012). Sedimentary pyrite. In Developments in sedimentology (Vol. 65, pp. 233–285). Elsevier. https://doi.org/10.1016/B978-0-444-52989-3.00006-4
Rickard, D., Mussmann, M., & Steadman, J. A. (2017). Sedimentary sulfides. *Elements*, *13*(2), 117–122. https://doi.org/10.2113/gselements.13.2.117
Robles, E. R., Fontan, F., Pesquera Pérez, A., & Keller, P. (1998). The Fe-Mn phosphate associations from the Pinilla de Fermoselle pegmatite, Zamora, Spain: Occurrence of kryzhanovskite and natrodufrénite. *European Journal of Mineralogy*, *10*(1), 155–168. https://doi.org/10.1127/ejm/10/1/0155
Rothe, M., Frederichs, T., Eder, M., Kleeberg, A., & Hupfer, M. (2014). Evidence for vivianite formation and its contribution to long-term phosphorus retention in a recent lake sediment: A novel analytical approach. *Biogeosciences*, *11*(18), 5169–5180. https://doi.org/10.5194/bg-11-5169-2014
Rothe, M., Kleeberg, A., & Hupfer, M. (2016). The occurrence, identification and environmental relevance of vivianite in waterlogged soils and aquatic sediments. *Earth-Science Reviews*, *158*, 51–64. https://doi.org/10.1016/j.earscirev.2016.04.008
Rust, G. W. (1935). Colloidal primary copper ores at Cornwall Mines, Southeastern Missouri. *The Journal of Geology*, *43*(4), 398–426. https://doi.org/10.1086/624318
Sawlowicz, Z. (1993). Pyrite framboids and their development: A new conceptual mechanism. *Geologische Rundschau*, *82*(1), 148–156. https://doi.org/10.1007/BF00563277
Sawłowicz, Z. (2000). *Framboids: From their origins to application = Framboidy: Od ich genezy do zastosowania (No. 88 = no. 88)*. Oddziału Polskiej Akademii Nauk.
Schallreuter, R. E. (1984). Framboidal pyrite in deep-sea sediments. In *Initial reports of the deep sea drilling project* (Vol. 75, pp. 875–891). U.S. Government Printing Office. https://doi.org/10.2973/dsdp.proc.75.124.1984
Schieber, J. (2002). Sedimentary pyrite: A window into the microbial past. *Geology*, *30*(6), 531. https://doi.org/10.1130/0091-7613(2002)030<0531:spawit>2.0.co;2
Schmid-Beurmann, P. (2000). Synthesis and phase characterization of a solid solution series between β-Fe2(PO4)O and Fe4(PO4)3(OH)3. *Journal of Solid State Chemistry*, *153*(2), 237–247. https://doi.org/10.1006/jssc.2000.8747
Schneiderhöhn, H. (1923). Chalkographische untersuchung des mansfelder kupferschiefers. *Neues Jahrbuch für Mineralogie, Geologie und Paläontologie*, *47*, 1–38.
Schoonen, M. A. (2004). Mechanisms of sedimentary pyrite formation. In *Sulfur biogeochemistry—Past and present*. Geological Society of America. https://doi.org/10.1130/0-8137-2379-5.117
Scott, R. J., Meffre, S., Woodhead, J., Gilbert, S. E., Berry, R. F., & y, P. (2009). Development of framboidal pyrite during diagenesis, low-grade regional metamorphism, and hydrothermal alteration. *Economic Geology*, *104*(8), 1143–1168. https://doi.org/10.2113/gsecongeo.104.8.1143
Shen, Y., Buick, R., & Canfield, D. E. (2001). Isotopic evidence for microbial sulphate reduction in the early Archaean era. *Nature*, *410*(6824), 77–81. https://doi.org/10.1038/35065071
Sim, M. S., Bosak, T., & Ono, S. (2011). Large sulfur isotope fractionation does not require disproportionation. *Science*, *333*(6038), 74–77. https://doi.org/10.1126/science.1205103
Sugawara, H., Sakakibara, M., Belton, D., & Suzuki, T. (2013). Formation process of pyrite polyframboid based on the heavy-metal analysis by micro-PIXE. *Environmental Earth Sciences*, *69*(3), 811–819. https://doi.org/10.1007/s12665-012-1966-7
Sweeney, R. E., & Kaplan, I. R. (1973). Pyrite framboid formation; Laboratory synthesis and marine sediments. *Economic Geology*, *68*(5), 618–634. https://doi.org/10.2113/gsecongeo.68.5.618
Tang, M., & Li, Y.-L. (2020). A complex assemblage of crystal habits of pyrite in the volcanic hot springs from Kamchatka, Russia: Implications for the mineral signature of life on Mars. *Crystals*, *10*(6), 535. https://doi.org/10.3390/cryst10060535
Taylor, K., & Macquaker, J. (2000). Early diagenetic pyrite morphology in a mudstone-dominated succession: The Lower Jurassic Cleveland Ironstone Formation, eastern England. *Sedimentary Geology*, *131*(1–2), 77–86. https://doi.org/10.1016/S0037-0738(00)00002-6
Thiel, J., Byrne, J. M., Kappler, A., Schink, B., & Pester, M. (2019). Pyrite formation from FeS and H_2S is mediated through microbial redox activity. *Proceedings of the National Academy of Sciences*, *116*(14), 6897–6902. https://doi.org/10.1073/pnas.1814412116
Tschech, A., & Pfennig, N. (1984). Growth yield increase linked to caffeate reduction in Acetobacterium woodii. *Archives of Microbiology*, *137*(2), 163–167. https://doi.org/10.1007/BF00414460
Vallentyne, J. R. (1963). Isolation of pyrite spherules from recent sediments. *Limnology & Oceanography*, *8*(1), 16–30. https://doi.org/10.4319/lo.1963.8.1.0016
Viennet, J.-C., Bernard, S., Le Guillou, C., Jacquemot, P., Balan, E., Delbes, L., et al. (2019). Experimental clues for detecting biosignatures on Mars. *Geochemical Perspectives Letters*, 28–33. https://doi.org/10.7185/geochemlet.1931
Viennet, J.-C., Bernard, S., Le Guillou, C., Jacquemot, P., Delbes, L., Balan, E., & Jaber, M. (2020). Influence of the nature of the gas phase on the degradation of RNA during fossilization processes. *Applied Clay Science*, *191*, 105616. https://doi.org/10.1016/j.clay.2020.105616
Vietti, L. A., Bailey, J. V., Fox, D. L., & Rogers, R. R. (2015). Rapid formation of framboidal sulfides on bone surfaces from a simulated marine carcass fall. *PALAIOS*, *30*(4), 327–334. https://doi.org/10.2110/palo.2014.027
Wacey, D., Kilburn, M. R., Saunders, M., Cliff, J., & Brasier, M. D. (2011). Microfossils of sulphur-metabolizing cells in 3.4-billion-year-old rocks of Western Australia. *Nature Geoscience*, *4*(10), 698–702. https://doi.org/10.1038/ngeo1238
Wacey, D., Kilburn, M. R., Saunders, M., Cliff, J. B., Kong, C., Liu, A. G., et al. (2015). Uncovering framboidal pyrite biogenicity using nano-scale CNorg mapping. *Geology*, *43*(1), 27–30. https://doi.org/10.1130/G36048.1
Wang, P., Huang, Y., Wang, C., Feng, Z., & Huang, Q. (2013). Pyrite morphology in the first member of the Late Cretaceous Qingshankou formation, Songliao Basin, Northeast China. *Palaeogeography, Palaeoclimatology, Palaeoecology*, *385*, 125–136. https://doi.org/10.1016/j.palaeo.2012.09.027
Wang, Q., & Morse, J. W. (1996). Pyrite formation under conditions approximating those in anoxic sediments I. Pathway and morphology. *Marine Chemistry*, *52*(2), 99–121. https://doi.org/10.1016/0304-4203(95)00082-8

Watanabe, Y., Farquhar, J., & Ohmoto, H. (2009). Anomalous fractionations of sulfur isotopes during thermochemical sulfate reduction. *Science*, *324*(5925), 370–373. https://doi.org/10.1126/science.1169289

Wei, H., Chen, D., Wang, J., Yu, H., & Tucker, M. E. (2012). Organic accumulation in the lower Chihsia Formation (Middle Permian) of South China: Constraints from pyrite morphology and multiple geochemical proxies. *Palaeogeography, Palaeoclimatology, Palaeoecology*, *353–355*, 73–86. https://doi.org/10.1016/j.palaeo.2012.07.005

Widdel, F., Kohring, G.-W., & Mayer, F. (1983). Studies on dissimilatory sulfate-reducing bacteria that decompose fatty acids: III. Characterization of the filamentous gliding Desulfonema limicola gen. nov. sp. nov., and Desulfonema magnum sp. nov. *Archives of Microbiology*, *134*(4), 286–294. https://doi.org/10.1007/BF00407804

Wilkin, R. T., & Arthur, M. A. (2001). Variations in pyrite texture, sulfur isotope composition, and iron systematics in the Black Sea: Evidence for Late Pleistocene to Holocene excursions of the o2-h2s redox transition. *Geochimica et Cosmochimica Acta*, *65*(9), 1399–1416. https://doi.org/10.1016/S0016-7037(01)00552-X

Wilkin, R. T., Arthur, M., & Dean, W. (1997). History of water-column anoxia in the Black Sea indicated by pyrite framboid size distributions. *Earth and Planetary Science Letters*, *148*(3–4), 517–525. https://doi.org/10.1016/S0012-821X(97)00053-8

Wilkin, R. T., & Barnes, H. L. (1997a). Formation processes of framboidal pyrite. *Geochimica et Cosmochimica Acta*, *61*(2), 323–339. https://doi.org/10.1016/S0016-7037(96)00320-1

Wilkin, R. T., & Barnes, H. L. (1997b). Pyrite formation in an anoxic estuarine basin. *American Journal of Science*, *297*(6), 620–650. https://doi.org/10.2475/ajs.297.6.620

Wilkin, R. T., Barnes, H., & Brantley, S. (1996). The size distribution of framboidal pyrite in modern sediments: An indicator of redox conditions. *Geochimica et Cosmochimica Acta*, *60*(20), 3897–3912. https://doi.org/10.1016/0016-7037(96)00209-8

Williams, K. H., Ntarlagiannis, D., Slater, L. D., Dohnalkova, A., Hubbard, S. S., & Banfield, J. F. (2005). Geophysical imaging of stimulated microbial biomineralization. *Environmental Science & Technology*, *39*(19), 7592–7600. https://doi.org/10.1021/es0504035

Włodek, A., Grochowina, A., Gołębiowska, B., & Pieczka, A. (2015). A phosphate-bearing pegmatite from Lutomia and its relationships to other pegmatites of the Góry Sowie Block, southwestern Poland. *Journal of Geosciences*, 45–72. https://doi.org/10.3190/jgeosci.185

Wolin, E., Wolin, M., & Wolfe, R. (1963). Formation of methane by bacterial extracts. *Journal of Biological Chemistry*, *238*(8), 2882–2886. https://doi.org/10.1016/S0021-9258(18)67912-8

Wolthers, M., Butler, I. B., Rickard, D., & Mason, P. R. D. (2005). Arsenic uptake by pyrite at ambient environmental conditions: A continuous-flow experiment. In P. A. O'Day, D. Vlassopoulos, X. Meng, & L. G. Benning (Eds.), *Advances in arsenic research* (Vol. 915, pp. 60–76). American Chemical Society. https://doi.org/10.1021/bk-2005-0915.ch005

Zhelezinskaia, I., Kaufman, A. J., Farquhar, J., & Cliff, J. (2014). Large sulfur isotope fractionations associated with Neoarchean microbial sulfate reduction. *Science*, *346*(6210), 742–744. https://doi.org/10.1126/science.1256211